PHOTONIC CRYSTAL POINT-SHIFT NANOLASERS WITH AND WITHOUT NANOSLOTS — DESIGN, FABRICATION, LASING AND SENSING CHARACTERISTICS —

Shota Kita, Kengo Nozaki, Shoji Hachuda, Hideki Watanabe, Yuji Saito, Shota Otsuka, Takeharu Nakada, Yoshiki Arita, and Toshihiko Baba, *Member, IEEE*

(Invited Paper)

***Abstract*— GaInAsP photonic crystal (PC) point-shift nanolasers operate at room temperature and under pulsed and continuous-wave condition by photopumping, with an effective threshold of ~1 μW, a single mode peak of over 40 dB, and a small modal volume of ~0.2 times the cubic wavelength. We report the details of its design, fabrication process, measurement method, and lasing characteristics. In particular, we reveal that wide spectral broadening often observed for nanolasers under pulsed condition is caused by large thermal chirping. Then, we focus on a nanolaser-based liquid index sensor, which is also applicable to detecting gases and bio-molecules. The dependence of the laser's sensitivity and resolution on the modal profile and spectral linewidth are investigated. We also configure the laser in a large-scale array, and demonstrate spectrometer-free sensor system. Finally, we present a nanoslot nanolaser, which is particularly suitable for further reducing the modal volume and enhancing light-matter interaction and sensor performance. Additionally, we demonstrate that high sensitivity and spectral narrowing by the unique optical confinement in the nanoslot gives rise to.**

***Index Terms*— Photonic crystal, nanolaser, GaInAsP, sensing, bio-photonics, nanoslot**

I. INTRODUCTION

With the recent progress of nano-photonics, dense photonic integration has become a crucial issue toward future large-scale advanced photonic systems. Microlasers consisting of photonic crystals [1]-[6] and whispering gallery mode cavities [7], [8] are anticipated to function as on-chip light sources, signal processing devices, quantum electrodynamics tools, sensor heads, and so on. For a wide range of applications, such microlasers are first required to operate under room temperature continuous-wave (cw) condition. Target wavelength λ depends on the application, but near-infrared around 1.55 μm is a good candidate, which can exploit mature materials such as GaInAsP [8] and various measurement tools for silica fiber communications. For dense integration, ultimate threshold reduction and the enhancement of light-matter interactions of microlasers, the modal volume V_m [1] has to be as small as possible; close to the diffraction limit. A moderately high Q of the laser cavity provides low threshold and efficient output. Q is limited by the diffraction loss with decreasing V_m, but the diffraction loss can be minimize by optimizing the cavity structure. Q is also limited by the scattering loss due to disordering of the structure and the free carrier absorption (FCA). While the scattering loss is a technical issue, the FCA is an essential constraint. Unlike passive cavities, Q in microlasers is limited by the FCA to tens of thousands in standard quantum-well (QW) microlasers. Therefore, the reduction of V_m becomes more challenging once the Q limited by the diffraction and scattering losses reaches the FCA limit.

In this paper, we discuss photonic crystal (PC) microlasers, which achieve a smallest V_m simultaneously with a sufficiently high Q. PCs are artificial mosaic structures having a periodicity comparable to λ [9], [10]. The PC slab consisting of high-index membrane perforated by airholes is the most common structure, which balances a useful pseudo photonic band-gap (PBG) and easy fabrication [1], [11]. Light is confined in the slab by total internal reflection, and an in-plane PBG occurs for the TE-like polarization. Microcavities are easily formed by removing and/or shifting some airholes. In comparison with other microlaser structures such as vertical cavities [12], [13], disks [8], [14]-[18], rings [17], [19], toroids [20], [21] and spheres [22], [23], well-optimized PC microlasers have achieve much

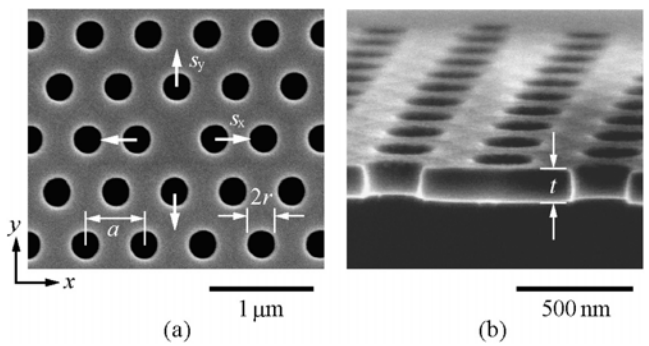

Fig. 1 Scanning electron micrograph (SEM) of fabricated GaInAsP PC H0 nanolaser. (a) Top view and coordinate system. (b) Side view.

Manuscript received November 30, 2010.

Authors are with the Department of Electrical and Computer Engineering, Yokohama National University, 79-5 Tokiwadai, Hodogaya-ku, Yokohama 240-8501, Japan (corresponding author to provide phone: +81-45-339-4258; fax: +81-45-338-1157; e-mail: baba@ynu.ac.jp).

S. Kita, K. Nozaki, H. Watanabe, T. Nakada and T. Baba are also with CREST, Japan Science and Technology Agency, 5 Sanbancho, Chiyoda-ku, Tokyo 102-0075, Japan

smaller V_m for the same Q; e.g. $V_m = 1.2(\lambda/n)^3$ for $Q = 1.9 \times 10^4$ [5], where n is the highest index of cavity media. This is attributed to the spatial Fourier analysis of PC microcavities, which visualizes leaky components of the cavity mode and allows the strategic optimization of the cavity [24]. Single-point defect PC cavities with one missing airhole (usually called H1) have a modal length shorter than 1 μm in all directions at $\lambda \sim 1.55$ μm, hence they should be called *nanocavity* and *nanolaser*. A nanolaser smaller than H1 can be formed only by shifting some neighboring airholes, as shown in Fig. 1. We call it *point-shift nanolaser* or *H0 nanolaser*, meaning no missing airholes [6], [25]-[30].

More than 10 years have passed since the first pulsed operation in PC nanolaser has been achieved. However, the room temperature cw operation is still limited, and large-scale integration, high-yield operation, and practical applications have not yet been investigated. Through on-going studies during this time, we are convinced that GaInAsP QW PC H0 nanolaser is one of the most promising candidates towards these issues. In this paper, we comprehensively report the detailed design, fabrication and measurement methods, laser characteristics, and sensor operation of H0 nanolaser. We also propose and demonstrate a device that includes a nanoslot structure, which provides unique light localization both inside and outside of the semiconductor and improves the sensor performance.

In Section II, we summarize the theoretical dependence of the cavity mode and laser characteristics on structural parameters. In Section III, we describe the fabrication process, focusing on hydrogen iodide (HI) inductively coupled plasma (ICP) reactive ion etching, which greatly simplifies the fabrication process. In Section IV, we present the measurement setup and the measured laser characteristics. In particular, we reveal that the broad spectrum often observed in nanolasers under pulsed condition arises from large thermal chirping. In Section V, we discuss the laser's sensor applications, showing the optimizations for high sensitivity and resolution. We demonstrate the performance of a single device as well as large-scale array configuration suitable for spectrometer-free sensor system. In Section VI, we present the nanoslot nanolaser. After showing its theoretical characteristics of unique light localization, we demonstrate high-quality fabrication of very narrow nanoslot and clear laser operation. We confirm the light localization experimentally and observe suppressed thermal chirping and enhanced sensitivity, which together give a much higher resolution in sensing.

II. Structure and Theoretical Characteristics

(a) Laser wafer

Since the active layer of laser wafer is perforated by airholes in PC slab micro/nanolasers, surface recombination of carriers at the airhole sidewalls must be suppressed. Many studies have employed GaInAsP QWs for low surface recombination velocity υ_s [16], [31] and (Ga)InAs quantum dots for low carrier diffusion to the etched sidewalls [32]. In this study, we employ GaInAsP QWs with 1% compressive strain, epitaxially grown on (100) InP. In addition to the low υ_s, the QWs have the following advantages: 1) commercial availability of high quality wafer, 2) polarized emission compatible with the PBG in PC slabs, 3) high modal gain and absorption, applicable not only for lasing but also for signal processing [27], and 4) active/passive integration possible by regrowth process [33], [34]. One severe issue with GaInAsP is the large thermal resistance of ~20 K·cm/W, which makes cw operation difficult. Most of PC slabs reported so far are cladded by air for the purpose of strong optical confinement. Therefore, the thermal resistance in GaInAsP PC slab micro/nanolasers is usually as high as 10^5 – 10^6 K/W [6], [35]. Therefore, μW-order low threshold is necessary for cw operation.

We proceed the discussion with two wafers: single quantum-well (SQW) wafer and 5QW wafer. Band lineups of these wafers used in our experiments are shown in Fig. 2. The total thickness of the GaInAsP layers, t, in these wafers are 0.18 μm and 0.24 μm, respectively. The main differences between these two for lasing are the optical confinement factor into QWs, Γ_{QW}, active volume V_a, and Q limited by the diffraction loss, Q_{dif}. The detail of Q_{dif} is discussed later. We mention here that Γ_{QW} affects the Q limited by the FCA, Q_{FCA}. It is expressed as

$$Q_{FCA} = (2\pi/\lambda_\ell)n_{eq}/(\Gamma_{QW}\alpha_{FCA}) \quad (1)$$

where λ_ℓ is the lasing wavelength, n_{eq} is the equivalent modal index, and α_{FCA} is the absorption coefficient of the FCA determined by the carrier density. Substituting $\lambda_\ell = 1.55$ μm, $n_{eq} = 4.0$, and $\Gamma_{QW} = 2.1\%$ for the SQW and 9.2% for the 5QW, as well as $\alpha_{FCA} = 60$ cm^{-1} for a carrier density of 3×10^{18} cm^{-3} into Eq. (1), Q_{FCA} is estimated to be 130,000 and 29,000, respectively, for the SQW and 5QW.

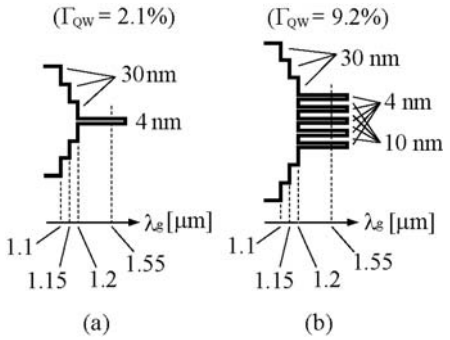

Fig. 2 Electronic band lineups of GaInAsP layers of two laser wafers considered and used in this study. (a) SQW wafer. (b) 5QW wafer. Γ_{QW} in this figure is calculated at $\lambda_\ell = 1.55$ μm assuming air cladding and index of GaInAsP with each electronic band-edge wavelength λ_g.

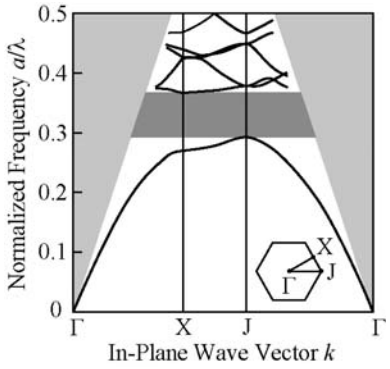

Fig. 3 Photonic band diagram of PC slab for TE-like polarization. Light and dark gray denote air light cone and PBG, respectively. Band curves close to the light cone are omitted because calculation accuracy is degraded by the deep modal penetration into air. The inset shows the in-plane Brillouin zone.

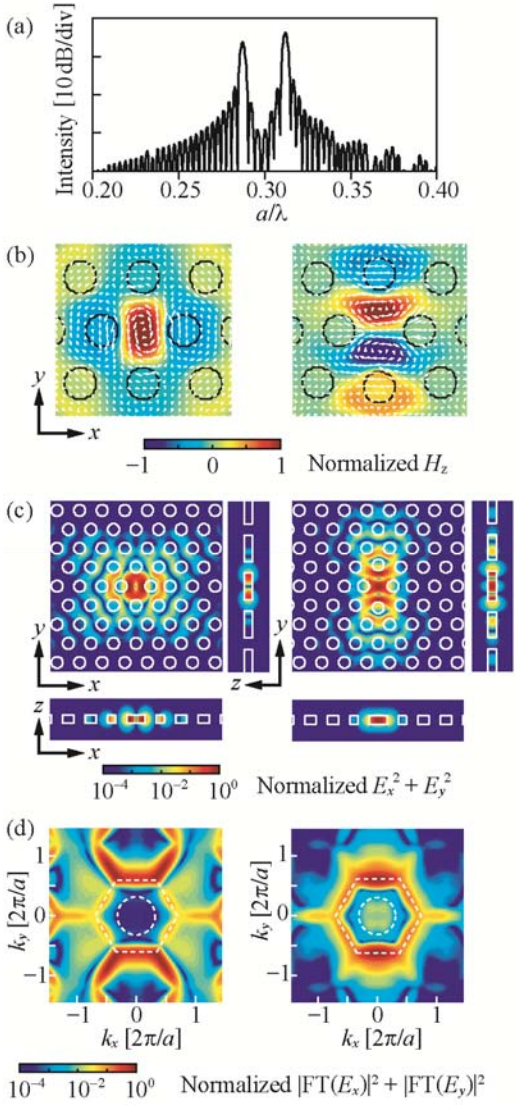

Fig. 4 FDTD calculation of (a) resonant spectrum, (b) in-plane distributions of modal electromagnetic fields (colors: H_z, arrows: $\boldsymbol{E}_{xy}$) at the slab center, (c) in-plane and center cross-sectional distributions of mode energy, and (d) Fourier transform (FT) of in-plane electric field. Left and right figures in (b) – (d) indicate monopole and dipole modes, and correspond to low and high frequency peaks in (a), respectively. Circular and hexagonal dotted lines in (d) denote the air light line and Brillouin zone, respectively.

(b) Cavity structure and modes

Fig. 3 shows the photonic bands for the TE-like polarization, calculated using three-dimensional (3D) plane-wave expansion method. A PC slab with a triangular lattice is assumed, with an average index of GaInAsP layers n_{slab} = 3.4, an index of air n_{air} = 1.0, a normalized airhole diameter $2r/a$ = 0.6, and a normalized slab thickness t/a = 0.32, where a is the lattice constant and $2r$ is the airhole diameter. The PBG lies at the normalized frequency a/λ = 0.29 – 0.36. It is known that larger $2r/a$ expands the PBG, but also expands the light cone of diffraction condition and degrades the Q_{dif}. The above $2r/a$ is value of appropriate to balancing them. Assuming the target a/λ_ℓ to be 0.30 – 0.36 and λ_ℓ = 1.55 μm, a is designed to be 0.47 – 0.56 μm, $2r$ = 0.28 – 0.34 μm, and t = 0.15 – 0.18 μm, respectively.

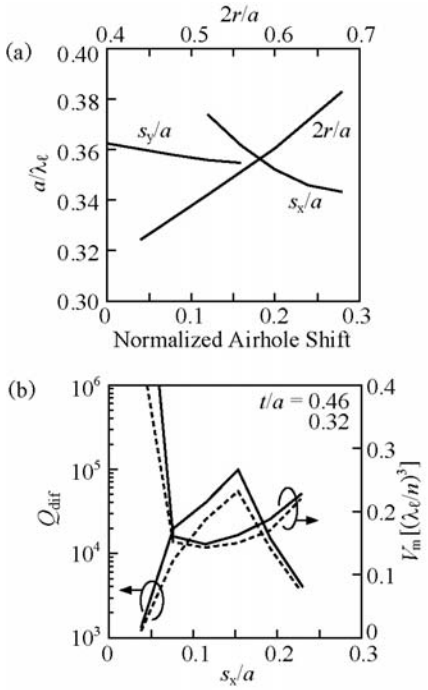

Fig. 5 Dependence of monopole mode characteristics of PC H0 nanocavity on structural parameters. (a) Normalized modal frequency a/λ_ℓ at t/a = 0.32. (b) Q_{dif} and V_m at t/a = 0.32 (dashed line) and 0.48 (solid line).

The H0 nanocavity is formed by shifting two adjacent airholes in the x direction by an amount s_x. Cavity modes can also be tuned by other shifts and diameter tuning. In this paper, we discuss the shift s_y of the other two airholes, in addition to s_x (see Fig. 1). Fig. 4 summarizes the resonant spectrum, field and energy distributions of two cavity modes, and their spatial Fourier transform, which are calculated by 3D finite-difference time-domain (FDTD) method. Here, we set the Yee cell size at 0.04a on each side (e.g. 20 nm at a = 0.50 μm), and assume s_x/a = 0.16 (80 nm) and s_y/a = 0 as well as $2r/a$ = 0.54 ($2r$ = 0.27μm) and t/a = 0.42 (t = 0.21 μm). Two resonant peaks on the low and high frequency sides in (a) correspond to monopole and dipole modes, respectively. Their gap divided by the midgap frequency is 0.067 in this case, but varies with airhole shifts s_x and s_y. The monopole mode in (b) has one major antinode of the vertical magnetic field H_z in the space between shifted airholes. Its field penetrates mainly in two of the Γ-X directions, as seen in (c), and the leaky components inside the white circle indicating the light cone in the Fourier spectrum (d) are well suppressed. The dipole mode has two major antinodes with larger penetration in another Γ-X direction, and the diffraction components are obviously larger than the monopole mode. This suggests that the monopole mode has a higher Q_{dif}. When PC waveguides are integrated with the nanocavity, optical coupling to each mode is possible by arranging the waveguides in different directions of the field penetration. This system will be effective for resonant pumping [29] and waveguide coupling [30], [33].

Fig. 5 shows the dependence of a/λ_ℓ, Q_{dif} and V_m of the monopole mode on structural parameters, while $2r/a$ = 0.6, s_x/a = 0.16, and s_y/a = 0 are fixed. The change in a/λ_ℓ is sensitive to $2r/a$ and s_x/a, and insensitive to s_y/a. Therefore, coarse and fine

tuning of frequency are possible by controlling them appropriately. It is particularly effective when integrating a large number of nanolasers at different wavelengths on a chip, as discussed in Section V. The highest Q_{dif} for t/a = 0.46 (e.g. t = 0.23 μm for a = 0.50 μm) is 1 × 10^5 at s_x/a = 0.16 (s_x = 80 nm). This value is comparable to the above-mentioned FCA limit for the SQW. When t/a = 0.32 (t = 0.16 μm), Q_{dif} decreases to 5 × 10^4 because a/λ becomes larger, the light cone is expanded, and the diffraction components increase. It is still very high, but slightly affects the threshold. For these t/a, V_m is less than $0.2(\lambda_\ell/n)^3$ in a wide range of s_x/a, and takes a minimum value of $0.14(\lambda_\ell/n)^3$ at s_x/a = 0.12 (s_x = 60 nm).

(c) Q dependencies of laser characteristics

Rate equations are solved for the carrier density $N(x,y)$ and the photon density S of the monopole mode, taking into account the surface recombination and carrier diffusion. We assume an active layer as in Fig. 2 (a = 0.52 μm, 2r = 0.26 μm), Gaussian circular photopump spot at λ = 0.98 μm with a $1/e^2$ diameter of 2.4 μm, and the same material parameters as those in [36]. We also assume that the modal profile and V_m = 0.019 μm^3 calculated by FDTD do not change with the carrier excitation, because the mode is strongly defined by the high-index contrast structure. We use the spontaneous emission factor multiplied by the Purcell factor, FC = 10, which we previously estimated from fitting the experimental mode intensity and lifetime characteristics with theory [6]. Regarding the pump power, we define three different values. The total irradiated power P_{irr} is given by integrating the Gaussian spot. The absorbed power P_{abs} is given by considering its imperfect absorption in the slab. The absorption coefficient at the pump wavelength is set at 20,000 cm^{-1}. The multi-reflection in the slab [15] is considered and pump light passing through airholes is excluded. It is calculated as $P_{abs} = 0.20P_{irr}$ for a = 0.52 μm, 2r = 0.26 μm and t = 0.18 μm. The effective pump power P_{eff} is estimated by counting further the spatial overlap of the pump spot with the effective modal area which is defined here as the central oval area inscribed to the shifted airholes. It is calculated as $0.12P_{abs}$ for the same a and 2r, s_x = 80 nm and s_y = 0 nm. The laser mode output P_{out} is calculated from $\eta\hbar\omega SV_a/\tau_{ph}$, where η is the external quantum efficiency defined as the sum of modal diffraction and scattering losses divided by the total loss including the FCA. τ_{ph} is the modal photon lifetime.

Fig. 6 shows the threshold power in P_{irr}, P_{abs}, and P_{eff} for the above a, 2r, s_x and s_y. The threshold is determined from the equal balance between the spontaneous and stimulated emissions. Here, we explicitly show the passive Q_{pas} as a parameter. It is defined as $(Q_{dif}^{-1} + Q_{scat}^{-1})^{-1}$, where Q_{scat} is that affected by the scattering loss. It means that Q_{pas} is degraded from Q_{dif} in Fig. 5(b) by the disordering in fabricated devices. The FCA is separately taken into account in the calculation. In general, the threshold decreases with the increase in Q_{pas}. When Q_{pas} < 2,000, the threshold of the 5QW device is lower due to higher gain of the wafer. For higher Q_{pas}, the threshold reduction is saturated by the FCA limit. In the SQW device, the gain is lower but the number of carriers for population inversion is also lower due to smaller V_a. The SQW wafer gives a lower threshold at Q_{pas} > 2,000 as the threshold gain is reduced. The saturation due to the FCW limit for this wafer becomes evident at $Q_{pas} > 10^4$.

Fig. 7(a) shows the P_{out} versus P_{eff} characteristics for SQW devices and the calculated distribution of $N(x,y)$ above threshold. Parameters are the same as for Fig. 6. Since the pump area is larger than the modal area, the spatial hole burning is clearly observed at the modal area, which limits the internal quantum efficiency. The semi-logarithmic plot in (a) shows the nonlinear rise of P_{out}. The threshold-less behavior is often discussed for nanolasers with large FC. However, P_{out} below threshold is not strong particularly in high Q_{pas} devices, because τ_{ph} extended by the high Q_{pas} accelerates the reabsorption of the laser mode [6]. The threshold-less behavior stands out for lower Q_{pas}, as seen more clearly in the log-log plots of (b). The rise point in (a) does not necessarily correspond to the threshold indicated by small dot on each curve; P_{out} can be

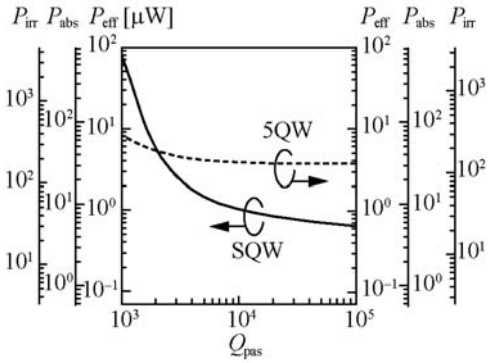

Fig. 6 Threshold power of PC H0 nanolaser calculated with Q_{pas}.

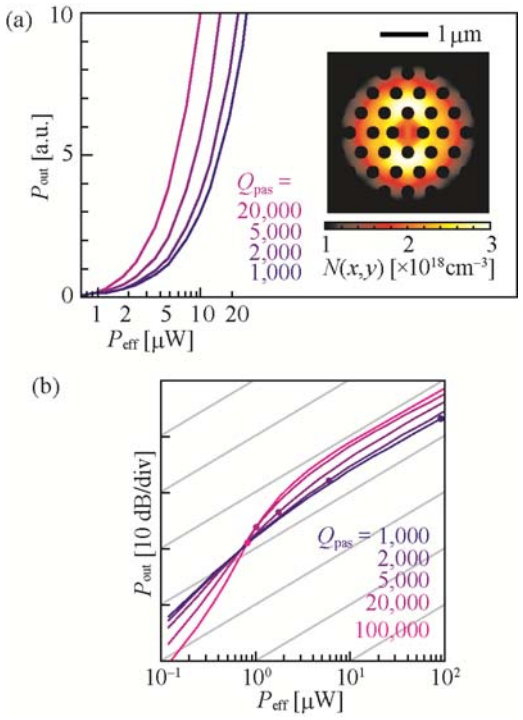

Fig. 7 P_{out} – P_{eff} characteristics calculated for SQW PC H0 nanolaser in (a) semi-log and (b) log-log plots. Inset in (a) displays calculated carrier distribution at $2P_{th}$ for Q_{pas} = 20,000. Small dot on each curve in (b) denotes calculated threshold. Thin hatched lines denote liner dependences.

sufficiently high when Q_{pas} is moderately low so that light extraction occurs quickly through the laser mode below threshold.

III. Fabrication

The SQW and 5QW wafers used here consist of GaInAsP layers grown on (100) InP substrate and cladded by 0.3 – 0.5 μm thick InP. PC patterns are formed into 0.3-μm-thick resist Zeon ZEP520A, using *e*-beam writer Elionix ELS7300 and ELS7500, with a gun voltage of 20 and 50 kV, respectively. We do not observe significant differences between them except for proximity effect and reproducibility. After post-baking the resist at 130°C, the semiconductor is directly etched using HI ICP reactive ion etching. After the etching, reactive products adsorbed on etched sidewalls are removed by diluted $(NH_3)_2S$ solution followed by conc-H_2SO_4, O_2 plasma ashing, and HF. The air-bridge PC slab is then formed by wet etching InP using HCl : H_2O = 4 : 1 at 3°C with a 1 μm/min etch rate.

For dry-etching GaInAsP/InP, chlorine-based gases are widely used. However, a high temperature of around 200°C is required for sufficiently high vapor pressure of indium chlorides. Therefore, a dielectric or metal medium is usually used as an etching mask, but this increases the process complexity and degrades the pattern accuracy. In contrast, HI allows room temperature etching with the resist mask, owing to high vapor pressure of indium iodides. Note that this etching is very sensitive to various condition and parameters. We particularly optimize them not for wide area patterns but for airholes of less than 0.3 μm diameter. The etcher is Samco RIE-200ip, whose chamber is made of aluminum covered with natural oxides. The sample is pasted on InP wafer using vacuum grease and set in the chamber using electrostatic force. The edge of the InP wafer is covered with alumina ring, so that only alumina and InP are exposed to the plasma. As alumina is not etched at all, no excrescent iodides are produced.

The detailed etching step is summarized in Table I. In the optimization procedure, we first observed that a high ICP power increases the edge roughness of the airholes. It may be due to local heating of the resist. Therefore, we employ a low ICP power of 100 W. In general, the aspect ratio and etching rate are improved by a high bias power. However, holes rapidly shrink toward the bottom when physical etching is dominant. Both physical and chemical etching are moderately controlled and the sidewall angle increases close to 90° by adjusting the gas pressure to 0.28 Pa with a bias power of 300 W. Regarding gas flow rate, a high value is usually preferred for evacuating reactive products quickly. However, severe side etching occurs at a HI flow rate over 1 sccm, which might be caused by incoming neutral radicals. The side etching is suppressed at a flow rate of 0.2 sccm. A small amount of Xe is first mixed in order to stabilize the plasma but stopped immediately because Xe stays behind for several tens of minutes during the etching process. The substrate temperature is set at 70ºC, which is much lower than the resist baking temperature. Fig. 8 shows the cross-sectional view of airholes after the etching when the resist is thickened to 1 μm and the etching time at #5 in Table I is extended to 2700 s as a demonstration of high-aspect deep etching. Etch rates of InP and resist are ~100 and ~10 nm/min. The former is almost the same as that for wide area patterns, but sidewalls of wide patterns are more tilted and the bottom is roughened. For GaInAsP layers, the average etch rate is approximately half of InP's. Note that excess side etching occurs for QWs at slightly higher temperature and lower bias power than the above. Careful control of these parameters is necessary to avoid this.

Fig. 9 shows the top view of 38 airholes fabricated nearby the shifted airholes, where colors display the distribution of 2*r*. When the target 2*r* is 0.22 μm or smaller, we only observe such random fluctuation regardless of the position of shifted airholes. The standard deviation is 2.4 nm. It is much smaller than > 10 nm observed for pure chlorine etching with a metal mask [35]. When the target is larger than 0.25 μm, the shifted airholes and their nearest neighbors are slightly expanded due to the proximity effect. The roughness σ at the slab surface and airhole sidewalls are smaller than 5 nm. For Si PC microcavities with σ < 2 nm, $Q > 2 \times 10^6$ has been reported [37]. Provided that Q_{scat} is proportional to σ^2 [38], we can expect $Q_{scat} > 10^5$ for

Table I Process steps of HI ICP etching.

Step	ICP Power [W]	Bias Power [W]	Gas Pressure [Pa]	HI Flow [sccm]	Xe Flow [sccm]	Temp. [℃]	Time [s]
#1	0	0	1.0	0.2	2	70	10
#2	100	0	2.0	0.2	2	70	7
#3	100	300	0.28	0.2	0	70	7
#4	100	300	0.28	0.2	0	70	7
#5	100	300	0.28	0.2	0	70	600

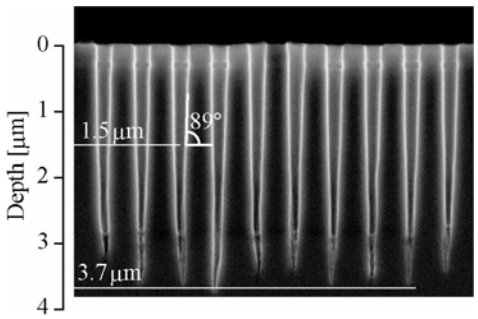

Fig. 8 Side SEM view of airholes demonstrating high-aspect etching of InP by using HI ICP etching with *e*-beam resist mask.

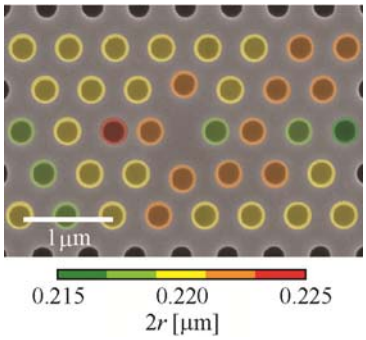

Fig. 9 Top SEM picture of GaInAsP PC H0 nanolaser (a = 0.50 μm, 2r = 0.22 μm, s_x = 80 nm, s_y = 60 nm). Color overlapping with each airhole denotes geometrically averaged 2r.

the σ < 5 nm roughness. As this value is comparable to or slightly higher than Q_{FCA}, the current process is already sufficient for the nanolaser. The slab thickness t after HCl etching varies in the range of 0.15 – 0.18 μm, although the total thickness of GaInAsP in the SQW wafer is 0.18 μm. This means that the outermost GaInAsP layer of λ_g = 1.1 μm is etched away slightly. In addition, the edge of airholes in the PC slab is sometimes rounded (see Fig. 1(b)). The HI etching might induce some damage at the GaInAsP-InP boundary and degrade the selectivity of the HCl etching. Q_{scat} could be degraded by these fabrication errors.

IV. Measurement

(a) Setup

Fig. 10 shows the schematic of the used measurement setup. For the photopump source, a 0.98 μm laser diode with single mode fiber output is used. It is driven under pulsed (75 ns pulse width, 10 kHz repetition frequency) or cw condition. Pump light is irradiated on the sample with a $1/e^2$ spot diameter of 2.4 μm through a 50× objective lens. Light output from the sample is collected by the same lens, and branched into optical spectrum analyzers (OSAs) Advantest Q8383/Q8384 and InGaAs infrared camera Indigo Alpha NIR through polished Si substrate as a filter of pump light. Transmission losses of the pump and detection paths are 13.8 dB at 0.98 μm and 10.6 dB at 1.55 μm, respectively. All the characteristics are measured at room temperature, except for temperature dependences, for which Peltier cooling and heating are used.

(b) Laser characteristics

Fig. 11(a) shows the P_{out}–P_{eff} characteristics measured for many samples of 5QW and SQW devices. 5QW devices only exhibit pulsed operation with a minimum threshold of P_{eff} = 5 μW. Based on the above theoretical and experimental studies, Q for 5QW devices is theoretically limited to 100,000, 100,000, and 29,000 each by Q_{dif}, Q_{scat}, and Q_{FCA}, respectively. Thus, the final Q and threshold are expected to be 18,000 and 4 μW, respectively (see Fig. 6). This threshold value is very close to

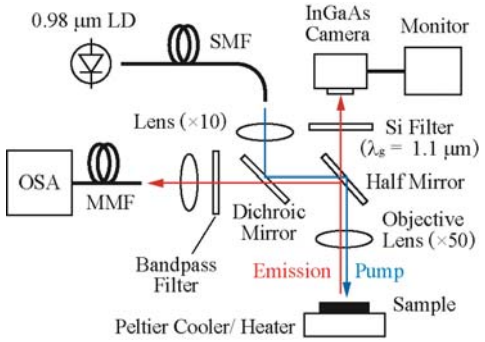

Fig. 10 Schematic of used measurement setup.

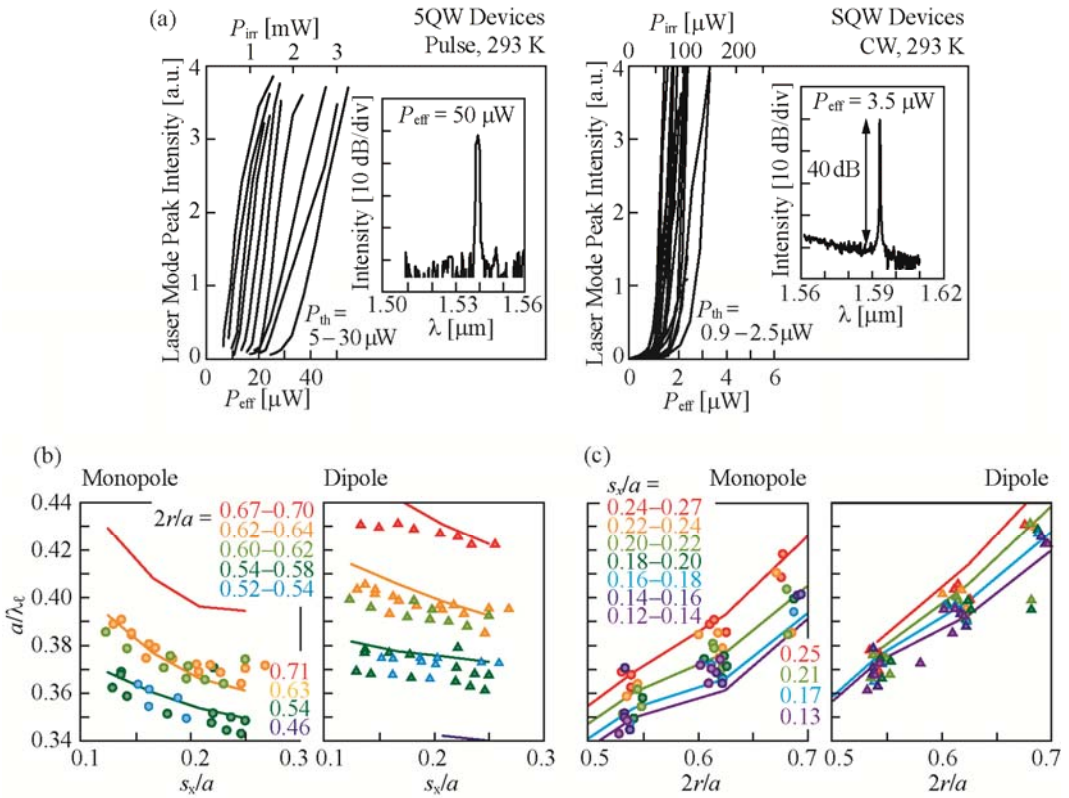

Fig. 11 Measured laser characteristics. (a) P_{out}–P_{eff} and P_{irr} plots for many samples and spectrum above threshold. P_{eff} is evaluated for each sample. P_{irr} is shown only for 5QW samples with a = 0.46 μm, $2r$ = 0.24 μm, s_x = 80 nm and s_y = 0 nm and for SQW samples with a = 0.56 μm, $2r$ = 0.28 μm, s_x = 100 nm and s_y = 0 nm. (b) a/λ_ℓ versus s_x/a characteristics for SQW devices. (c) a/λ_ℓ versus $2r/a$ characteristics for SQW devices. For (b) and (c), lines show theoretical values and circular and triangular plots show experimental values. Upper and lower values in these figures correspond to parameters in the theory and experiment, respectively.

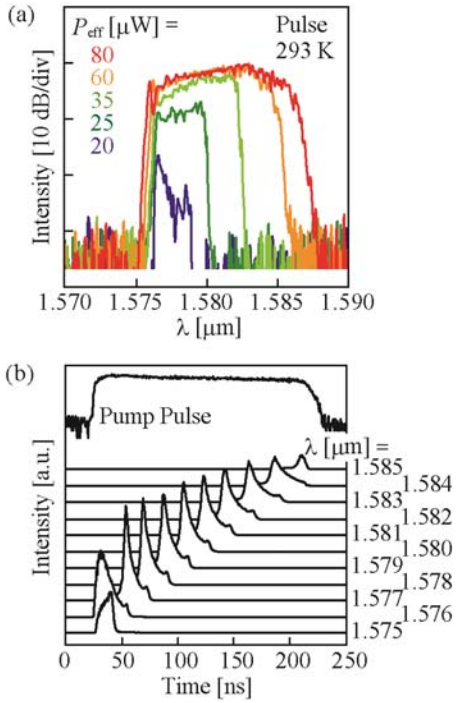

Fig. 12 Detailed observation of pulsed lasing spectrum. (a) Spectra for different P_{eff}, where pulse width is 500 ns and resolution of OSA is 0.2 nm. (b) Time-resolved spectral behavior observed using photomultiplier tube Hamamatsu, R5509-72, with a sub-100 ps response time and spectrometer with a 2 nm resolution. The pump pulse is also shown in log scale.

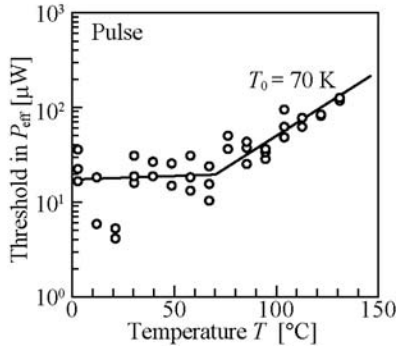

Fig. 13 Temperature dependence of threshold in P_{eff} under pulsed condition.

the experimental one. Since the device is heated even under pulsed operation, as discussed later, the output saturates at 3 – 4P_{th}, and the spectrum in the inset becomes broad although the peak intensity is >35 dB higher than the background noise level.

On the other hand, SQW devices exhibit both pulsed and cw operation with a minimum threshold of P_{eff} = 0.9 μW. In this case, Q is theoretically degraded to 50,000, 100,000 and 130,000 each by the three losses, respectively. It leads to a final Q of 26,000 and a threshold of 0.8 μW, which is also close to the experimental minimum. The maximum threshold for the cw operation is 2.5 μW, for which the corresponding Q is to be3,000. Light output increases rapidly above threshold and the laser characteristics similar to Fig. 7 are observed. The inset shows a spectral peak above threshold with an intensity 40 dB higher than the background spontaneous emission, which is

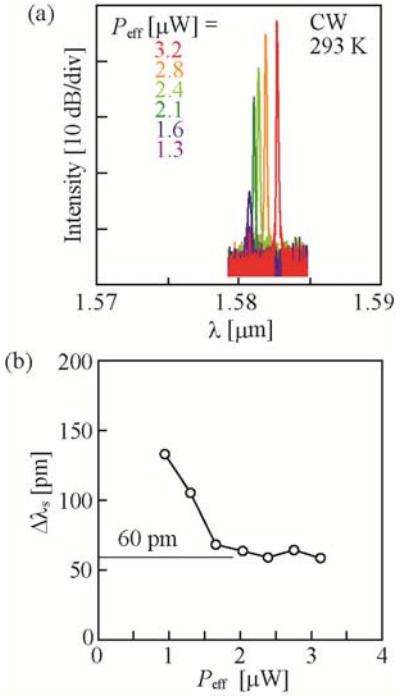

Fig. 14 Detailed observation of cw lasing spectrum. (a) Spectra for different P_{eff}. (b) Linewidth $\Delta\lambda_s$ with P_{eff}, where P_{th} is 1.7 μW for this device.

sufficient to confirm the laser operation. Figs. 11(b) and (c) summarize the measured a/λ_ℓ of monopole and dipole modes as functions of s_x/a and $2r/a$, respectively. Here, cw lasing in the dipole mode was not confirmed from weak peak intensity of around 10 dB, so resonant emission peaks are plotted. In general, enlarging $2r/a$ and decreasing s_x/a shrink the cavity area and shorten the laser/resonant wavelength. Calculated lines are in good agreement with experimental plots. This indicates that laser modes shown in Fig. 4 were actually obtained in this experiment.

(c) Spectral behaviors

Fig. 12(a) shows lasing spectra for different pump powers under pulsed condition. As P_{eff} increases, the longer wavelength side broadens very widely while the shorter side broadens only slightly; the broadening reaches to 10 nm at P_{eff} > 60 μW. In the past, such broadening had been associated with enhanced relaxation oscillation and self-pulsation [39]. However, we found that it is actually due to large thermal chirping in the thermally resistive nanolaser [40]. This is confirmed from time-resolved laser spectra, as shown in (b). In the duration of pump pulse, the spectrum first blue-shifts slightly and then red-shifts continuously with a response time of ~100 ns. We can explain that the blue and red-shifts are caused by carrier plasma and thermo-optic (TO) effects, respectively. Provided that the TO effect in GaInAsP devices is 0.11 nm/K [41], the 10 nm redshift corresponds to a temperature of ~110°C. One may suspect whether the nanolaser really maintains lasing at such a high temperature. However, the prospect is supported by the temperature characteristics measured by heating the sample holder, as shown in Fig. 13. The laser operation is observed up to 130°C. The characteristic temperature T_0 over 80°C is 70 K, which is a good value for GaInAsP lasers. We believe it is

attributed to the large Γ_{QW} in the air-clad PC slab giving strong optical confinement and a high modal gain.

Since the dynamic chirping is neglected under cw condition, the spectrum exhibits a much narrower linewidth $\Delta\lambda_s$, as shown in Fig. 14. $\Delta\lambda_s$ is decreased and saturated at 60 pm with increasing P_{eff}. This final value is wider than the 10 pm resolution limit of our Q8384 OSA. Small thermal fluctuation of ~0.5 K should broaden the spectrum. In fact, heating is confirmed from the red-shift of lasing peak against higher P_{eff}. Considering the absorbed pump power P_{abs}, the power dependence of the red-shift is estimated to be 0.13 nm/μW. From the above temperature dependence, the thermal resistance is estimated to be 1.5 × 10^6 K/W, which is almost the same as evaluated previously [15]. Since P_{abs} for the highest threshold device is calculated to be 25 μW, the device would be heated to ~60°C even at threshold.

V. Index Sensing

(a) Single device

If air cladding of the nanolaser is replaced by another soft medium such as gases and liquids, the modal index increases and the laser wavelength redshifts by $\Delta\lambda_\ell$. Correspondingly, we can estimate the environmental index n_{env} from $\Delta\lambda_\ell$ [42]. The mode is mainly confined in the slab, but the evanescent field penetrates into the airholes and the upper and lower claddings. For example, the 1/*e* penetration depth of the field in water is calculated to be 0.11 – 0.14 μm for the above nanolaser with t/a = 0.24 – 0.56. Since target media within this depth is selectively detected, it is also effective for sensing a thin bio-molecule layer adsorbed on the surface and sidewalls [19], [21], [43], [55], [59].

We define the index resolution of the sensor, Δn_{res}, in refractive index units (RIU) as [28]

$$\Delta n_{res} = \Delta\lambda_s/(\Delta\lambda_\ell/\Delta n_{env}) \quad (2)$$

where $\Delta\lambda_\ell/\Delta n_{env}$ denotes the sensitivity. There are a number of reports on sensors based on similar resonant wavelength shift in passive micro/nanocavities. In comparison, nanolasers have the following three advantages:

1) $\Delta\lambda_s$ is automatically narrowed by the laser oscillation. This eliminates the constraint between the device size and *Q* factor in passive cavities and the instability of passive *Q* easily affected by the disordering.
2) Optical input and output (I/O) are simplified since both the photopumping and the detection of laser emission can be done using free-space optics. This allows the separation of sensor chip and other measurement tools, and the production of low cost disposal sensor chips. This is not easy for passive cavities as they usually need fiber-coupled optical I/O, leading complicated process and high cost.
3) Coarse and fine observation can be mixed by changing the span and resolution for high-speed spectral analysis. It is not easy when a resonant mode in high *Q* passive cavities is searched by scanning the wavelength of tunable laser source.

One may be anxious about the fabrication process of nanolasers using *e*-beam lithography, which can be low-throughput and high-cost. However, it is not a problem actually. The device chip separated from other tools is very simple, so its fabrication is straightforward. The lithography area is very small for each chip and other process flow is also limited. Our rough estimate suggests that the chip cost is negligible compared with the cost of total sensor system.

Fig. 15 summarizes the calculated sensing characteristics. (a) shows $\Delta\lambda_\ell$ and Q_{dif} of the monopole and dipole modes of the H0 nanolaser, as well as those of the H1 [44], [45], calculated as a function of n_{env}. Here, the absorption of the environmental medium is not considered. λ_ℓ redshifts almost linearly and Q_{dif} decreases exponentially with increasing n_{env}. In the range of n_{env} = 1.3 – 1.4, which is typical of liquids, the H0 monopole mode simultaneously achieves a sensitivity of 320 nm/RIU and $Q_{dif} > 10^4$, both of which are larger than the H1's. This is attributed to the H0 cavity optimized by the spatial Fourier analysis. The dipole mode exhibits a higher sensitivity of 430 nm/RIU due to deeper field penetration, but its Q_{dif} is much lower than others. (b) shows the sensitivity and *Q* of two H0

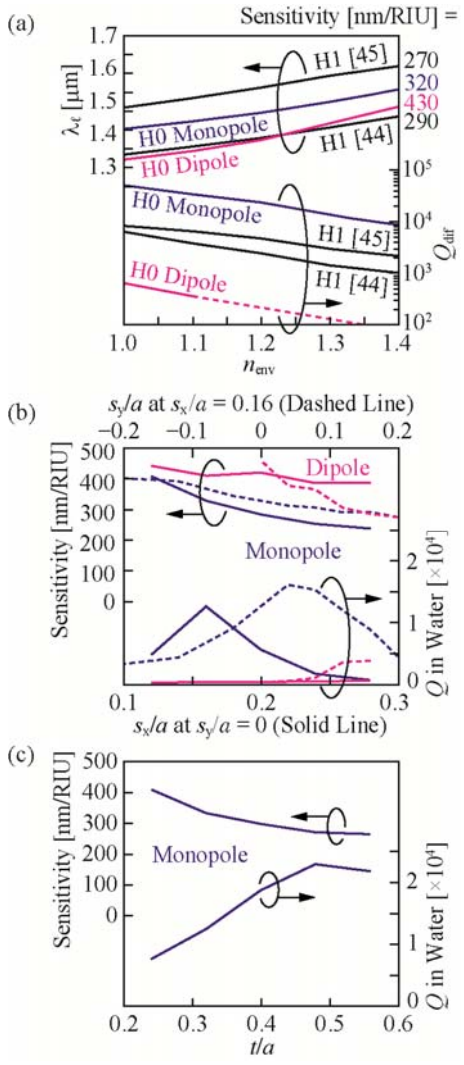

Fig. 15 Calculated sensing characteristics of PC H0 nanolaser. (a) λ_ℓ and Q_{dif} as a function of n_{env}. Those of H1 nanolaser [44], [45] are also shown for comparison. (b) Sensitivity and *Q* in water as functions of airhole shifts. (c) Sensitivity and *Q* in water as a function of normalized slab thickness. In each calculation, parameters not particularly shown are set as $2r/a$ = 0.52, s_x/a = 0.16, s_y/a = 0 and t/a = 0.32.

modes, calculated as functions of normalized airhole shifts. Here, water (n_{env} = 1.321) is assumed as the environmental medium. It degrades Q in the same manner as FCA because it has an absorption coefficient of 6.72 – 28.8 cm^{-1} at λ = 1.4 – 1.6 μm [46]. Overall, the dipole mode exhibits a higher sensitivity but a much lower Q. When s_y/a is larger than 0.12, Q of this mode is improved to higher than 3,000. However, it is noticed in this calculation that, for such large s_y/a, wavelengths of these two modes become closer, and enhance the possibility of multimode lasing and mode hopping. To avoid this undesirable situation for sensing applications, s_y/a must be smaller than 0.1. For the monopole mode, a higher sensitivity is obtainable with smaller shifts. However, Q will be lower than 5,000 because the field penetration enhanced by the smaller shifts results in stronger absorption in water. Q is maximized up to 16,000 in water, when s_x/a = 0.16 and s_y/a = 0.02. In this condition, a sensitivity higher than 300 nm/RIU is expected. (c) shows the sensitivity and Q of the monopole mode in water, calculated as a function of normalized slab thickness. If the slab is thinned to t/a = 0.22, the sensitivity is enhanced to 410 nm/RIU, maintaining Q > 7,000. For t/a = 0.30 – 0.36 in our experiment, we can expect 320 – 280 nm/RIU, respectively.

In evaluating the experimental Δn_{res}, we used standard index liquids Cargille B0700/0701 with an index range of 1.296 – 1.451. The liquid is dropped on the device, a cover glass put on, and photopumped. Fig. 16(a) shows cw lasing spectra against various liquids. Very clear single mode peak is maintained with a maximum peak intensity of 50 dB above the spontaneous emission level. It is attributed to the heat sink effect of liquids having at least five-fold higher thermal conductivity than air. The minimum $\Delta\lambda_s$ measured in this experiment is 26 pm. It is smaller than that in Fig. 14(b) but still larger than the resolution limit of OSA. Even in liquid, the thermal fluctuation issue remains. In fact, we observe convection and sometimes boiling of the liquid during the cw operation, particularly when the liquid is water and the device surface is hydrophobic. From Fig. 16(a), the sensitivity is estimated to be 280 nm/RIU. It is approximately the same as that expected from Fig. 15. These $\Delta\lambda_s$ and sensitivity give $\Delta n_{res} = 9.3 \times 10^{-5}$ RIU. This value could be improved by suppressing the thermal fluctuation and using higher resolution OSA. Fig. 16(b) shows experimental sensitivity with s_x/a for two modes, where those of different lot samples with s_y/a = 0 – 0.12 and t/a = 0.28 – 0.36 are plotted together. Some plots of the dipole mode are obtained for resonant emission peaks as we could not confirm the cw lasing. These plots roughly correspond to calculated results in Fig. 15(b). The maximum sensitivity is 330 and 460 nm/RIU for the monopole and dipole modes, respectively, which were obtained for thinner slab samples. Some devices exhibit sensitivities as low as 150 – 230 nm/RIU, which are not expected in Fig. 15. It has been reported that residual air around the airholes degrades the sensitivity [45]. This is also true in our experiment. Actually, we sometimes observe that the liquid does not infiltrate sufficiently underneath the slab when the device surface is hydrophobic after HCl etching. Such situation will be improved by chemical pre-treatment for making the surface hydrophilic and/or by opening larger holes around the PC to release the air.

In this experiment, we also tested the pulsed pumping. It this case, the large spectral broadening in Fig. 12 is suppressed

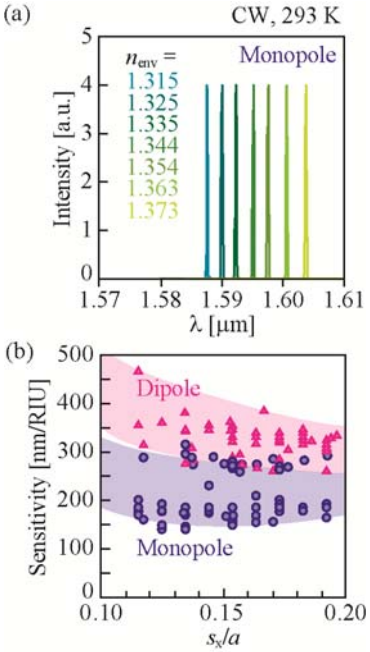

Fig. 16 Liquid index sensing using H0 nanolaser with s_x = 80 nm, s_y = 40 nm, and t = 0.18 μm under cw condition. (a) Spectral shift for different index liquids. (b) Sensitivity measured for many samples with different s_x/a.

to 0.5 – 1 nm in a liquid. This result supports again our consideration that the spectral broadening is caused by the thermal chirping and that the liquid is effective for heat sinking. The 0.5 – 1 nm broadening corresponds to a temperature rise of 4 – 9 K during the pumping. This broadening is not acceptable for high resolution sensing, but can be suppressed by a nanoslot structure, as discussed in the next section. The reduced temperature rise is preferable for stabilizing the condition of liquid. It will also be effective for sensing bio-materials, which is sensitive to and damaged by strong heating.

(b) Array configuration

To simplify the overall sensing system including nanolasers and OSA, we have proposed a large-scale array configuration, as illustrated in Fig. 17 [28]. For example, it is possible to integrate more than 1,000 nanolasers within a (100 μm)^2 area, if they are arranged two-dimensionally with a 3 μm period. These nanolasers are designed to have different λ_ℓ. They are operated simultaneously and their emission are observed as a spot pattern by using infrared camera through band-pass filter (BPF) having a step-like spectral response. If λ_ℓ is changed gradually along the order of nanolasers, the dot pattern simply shifts before and after dropping a liquid on the device, and n_{env} is obtained from this shift. λ_ℓ is not necessarily changed gradually. Even if it is changed randomly, n_{env} can be estimated after pre-measuring the correspondence between spot patterns and n_{env} like two-dimensional matrix bar codes. Thus, it acts as a spectrometer-free index sensor.

In this method, the resolution Δn_{res} is given by

$$\Delta n_{res} = \Delta\lambda_X/(\Delta\lambda_\ell/\Delta n_{env}) \quad (3)$$

where $\Delta\lambda_X$ is the wavelength uncertainty at the boundary between bright and dark spots. The uncertainty is caused by the largest value between the linewidth $\Delta\lambda_s$, the nearest wavelength

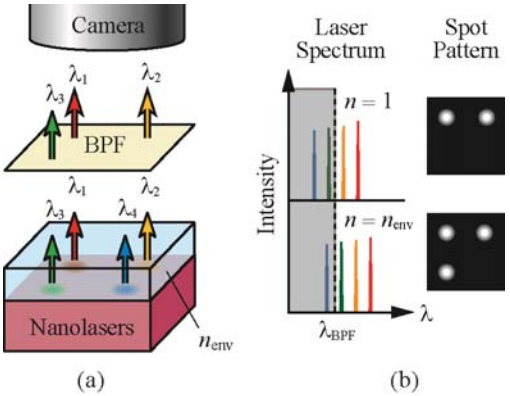

Fig.17 Schematics of spectrometer-free index sensing using nanolaser array. (a) Total setup. (b) Relation of laser spectra and spot pattern observed through BPF.

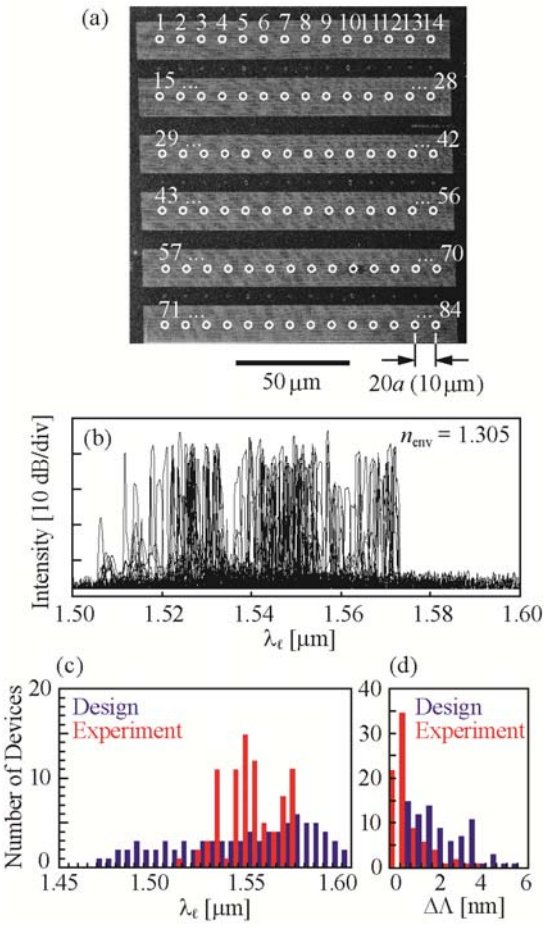

Fig. 18 Fabricated nanolaser array. (a) SEM picture of the device. White circle indicates the position of each nanolaser. (b) Observed emission spectra of 84 devices in index liquid. (c), (d) Histogram of measured λ_ℓ and $\Delta\Lambda$ compared with those expected from cavity design.

spacing between nanolasers, $\Delta\Lambda$, and the intensity fluctuation converted by the BPF response, $(\Delta I/I)/(\Delta T/\Delta\lambda)$. Here, $\Delta I/I$ is the fluctuation in spot intensity induced from the pump source, nanolaser, and camera. $\Delta T/\Delta\lambda$ is the spectral slope of the BPF at a 50% transmittance. Let us consider the case of our cw nanolaser showing $\Delta\lambda_s$ = 26 pm and $\Delta\lambda_\ell/\Delta n_{env}$ = 280 nm/RIU, and assume reasonable values of $\Delta I/I$ = 0.01 and $\Delta T/\Delta\lambda = (6\ \text{nm})^{-1}$.

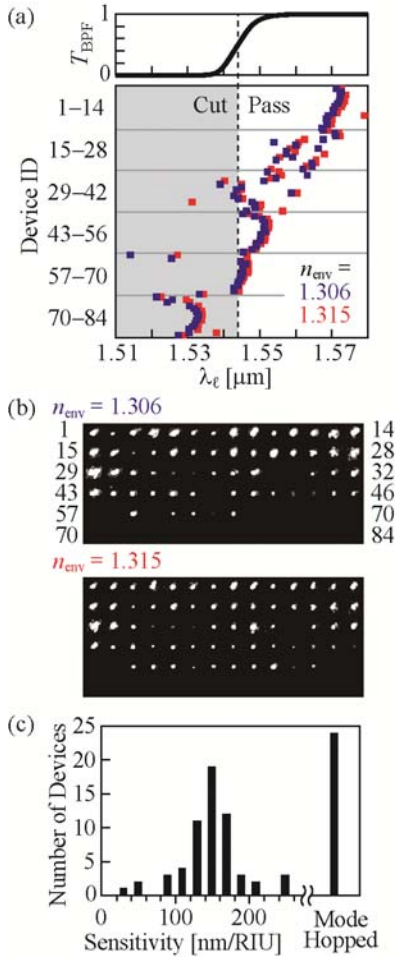

Fig. 19 Spectrometer-free sensing operation using nanolaser array. (a) Distribution of λ_ℓ measured using OSA and its variation against different liquids. Spectral response of used BPF, T_{BPF}, is also shown. (b) Variation of spot pattern for different index liquids. (c) Histogram of index sensitivity.

Then, $(\Delta I/I)/(\Delta T/\Delta\lambda)$ becomes 60 pm, which is larger than $\Delta\lambda_s$. If we can set $\Delta\Lambda$ to be smaller than this value, Δn_{res} becomes 2.1 × 10^{-4} RIU. It would be a crucial issue, however, whether such a small $\Delta\Lambda$ is obtainable uniformly or not. Nonuniformity in $\Delta\Lambda$ results in erratic resolution.

Fig. 18(a) shows the top view of fabricated nanolaser array. Here, 14 devices with a = 0.5 μm and s_x = 60 – 125 nm (5 nm steps) are aligned in the x direction. Here, s_y is designed to be 40 nm, because a small s_y shift improves the Q of monopole mode, as shown in Fig. 15(b). The period of the alignment is set as wide as $20a$ = 10 μm so that neighboring emission are observed separately (if we do not care for this point, we can reduce the period to less than 3 μm). In addition, six rows of such one-dimensional array are aligned in the y direction with varying $2r$ from 0.215 – 0.240 μm (5 nm steps). In total, 84 devices are integrated within a 150 × 150 μm area, which corresponds to a field size of e-beam lithography. The step size of 5 nm in s_x and $2r$ are determined by the minimum possible values of lithographic parameters. Fig. 6(a) indicates that the minimum step in s_x and $2r$ will provide $\Delta\lambda_\ell$ = 5 – 7 nm and 10 nm, respectively, and that λ_ℓ will be in the range of 1.46 – 1.60 μm. In this preliminary measurement, we scanned the pump

spot along the nanolasers and obtained the laser spectra, as shown in Fig. 18(b). All the devices exhibit laser or resonant emission peak with sufficiently strong intensity. Here, the pumping is performed under pulsed condition to acquire high yield lasing, so $\Delta\lambda_s$ = 0.5 – 1 nm in liquids. Histograms of measured λ_ℓ and $\Delta\Lambda$ are shown in Figs. 18(c) and (d). λ_ℓ is distributed in the range of 1.50 – 1.57 μm, which is narrower than the designed range. More than 60 devices exhibit $\Delta\Lambda < 0.6$ nm and other devices show $\Delta\Lambda$ up to several nanometers. The narrow range of λ_ℓ and the nonuniform $\Delta\Lambda$ are mainly caused by the proximity effect in the *e*-beam lithography particularly around the shifted airholes. The wavelength shift due to s_x tuning is partially canceled by the increase in 2*r* from the proximity effect as mentioned in Section III.

Sensing operation of the nanolaser array is summarized in Fig. 19. (a) shows the spectral response of the used BPF, where the slope at 50% transmittance is $(6\ \text{nm})^{-1}$, and the distribution of λ_ℓ of all the devices measured by OSA. Except for device ID 15 – 42 and some others, the measured λ_ℓ changes linearly with position. Blue and red plots show the wavelength shift against different liquids. 24 devices exhibit unexpected wide wavelength shifts caused by mode hopping. Other devices show reasonably small shifts, which can be used for sensing operation. Accordingly, the spot pattern changes, as show in (b). As n_{env} increases, the number of spots increases particularly on the line of ID 57 – 70. Thus, the spectrometer-free sensing is demonstrated. The sensitivity of all devices are summarized in (c). The average sensitivity is 150 nm/RIU. It may be caused by the insufficient infiltration of the liquid, as mentioned above. From $\Delta\Lambda < 0.6$ nm for 60 devices, $\Delta\lambda_s$ = 0.5 – 1 nm, and $\Delta\lambda_\ell/\Delta n_{env}$ = 100 – 200 nm/RIU, Δn_{res} is estimated to be 2.5 – 10 $\times 10^{-3}$ RIU. On the other hand, 4 – 6 spots at ID 57 – 70 turn on after changing n_{env} by 0.009, giving $\Delta n_{res} = 2.2 – 1.5 \times 10^{-3}$ RIU. Thus rough correspondence is confirmed.

The linewidth $\Delta\lambda_s$ is narrowed to less than 0.1 nm by employing a nanoslot, as shown in the next section. The mode hopping will be suppressed by controlling s_y more carefully and reducing the *Q* factor of the dipole mode. $\Delta\Lambda < 0.6$ nm is expected with sufficient uniformity by suppressing the proximity effect. The sensitivity will be enhanced up to 300 nm/RIU by removing residual air. Therefore, we believe $\Delta n_{res} < 2 \times 10^{-3}$ RIU is practically anticipated even with the present technology. It is sufficient to distinguish common liquids such as water and alcohol and also some bio-samples such as large size proteins. Essential and/or technological improvements are necessary for quantitative analysis of mixed liquids and molecular level detection of bio-samples.

VI. Nanoslot Nanolaser

(a) Structure and theory

The smallest limit of V_m in dielectric cavities is fundamentally dominated by the diffraction limit. A hint that breaks this limit is suggested by a slotted waveguide, in which a low-index nanoslot (NS) is embedded between two high-index waveguides [47]-[49]. In such a waveguide, the optical field is enhanced and confined in the NS even when light is guided by total internal reflection. Such anomalous enhancement and confinement are explained as follows. For a high-index contrast interface, Maxwell's equations dictate that, in order to satisfy the continuity of the normal component of electric flux density ***D***, the corresponding ***E*** field must undergo a large discontinuity with a much higher amplitude in the low-index side. This discontinuity can be used to strongly enhance the field in the low-index NS. Recently, NS structures have been investigated in a light emitter based on an Er-doped silicon waveguide [49] and in one-dimensional PC cavities [50]. Here, we propose to form a NS in the PC H0 nanolaser. Since the electric energy of the monopole mode in the H0 nanolaser is dominated by the *y*-polarized component (see Fig. 4(b), (c)), the NS along the *x* direction is adequate for the above mechanism of light localization. Fig. 20 shows the 3D FDTD calculation of electric field energy distribution $\varepsilon|E|^2$ with and without the NS. Values of $\varepsilon|E|^2$ in (a) – (c) are normalized so that their spatial integrals are equal. The NS width w_{NS} is fixed at $w_{NS}/a = 0.04$ (e.g. w_{NS} =20 nm at a =0.5 μm). The NS depth d_{NS} is changed such that

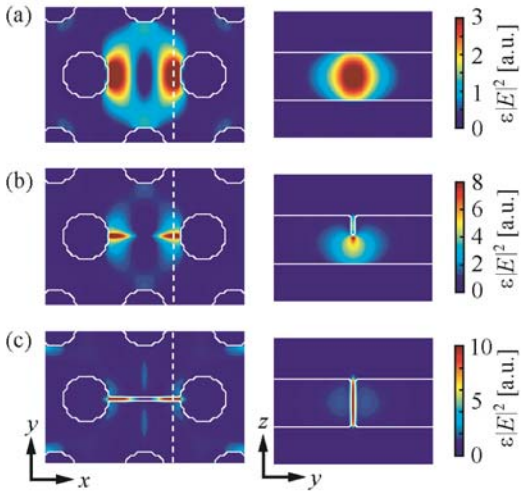

Fig. 20 Calculated electric field energy of monopole mode in PC H0 nanolaser with normalized NS depth d/t = (a) 0, (b) 0.4, and (c) 1.0. Left shows *xy* profiles at slab center. Right shows cross-sectional profiles on dashed line of left figures. Parameters are the same as those in Fig. 5.

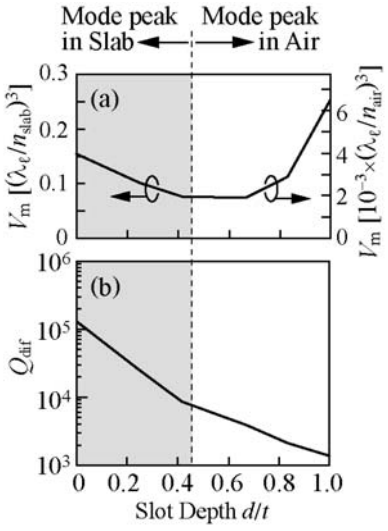

Fig. 21 Modal volume (a) and Q_{dif} (b) calculated with normalized NS depth in air. Parameters are the same as those in Figs. 5 and 20.

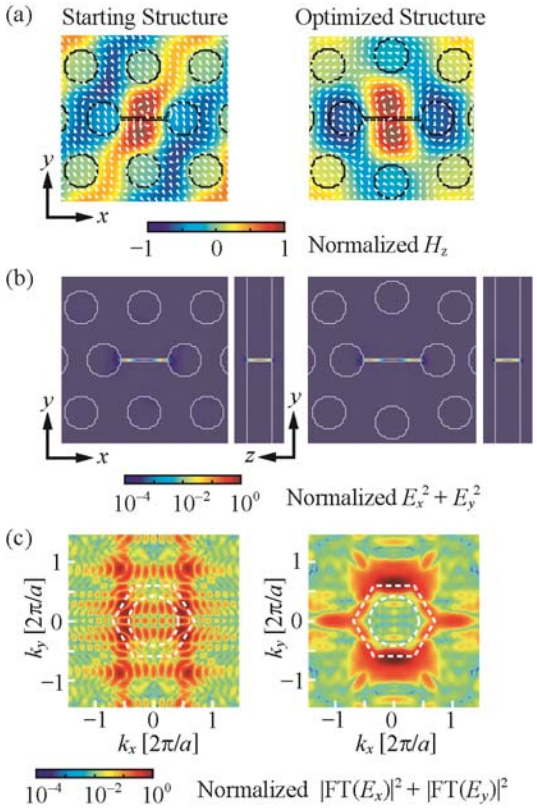

Fig. 22 FDTD calculation of (a) in-plane distributions of modal electromagnetic fields (colors: H_z, arrows: $\boldsymbol{E}_{xy}$), (b) in-plane and central cross-sectional distributions of modal energy, and (c) the FT of the in-plane electric field for NS H0 nanolaser in water (n_{water} = 1.321 is assumed). Left and right figures denote those of a starting structure (s_x/a = 0.16, s_y/a = 0) and optimized structure (s_x/a = 0.24, s_y/a = 0.08), respectively. Circular and hexagonal dotted lines in (c) denote the air light line and Brillouin zone, respectively. $2r/a$ = 0.52, t/a = 0.4 and w_{NS}/a = 0.04.

d_{NS}/t = 0, 0.4, and 1.0. When the NS is formed close to the middle the slab, as shown in (b), the energy peak is located inside the semiconductor just below the NS. Here, peak values of $\varepsilon|E|^2$ and $|E|$ are enhanced by a factor of 2.5 and 1.6, respectively, compared the case without the NS. Such an enhancement can be explained as follows. The E_y component in the NS is enhanced by the mechanism mentioned above. It is continuously penetrating to the semiconductor at the bottom of the NS, while penetrating D_y is enhanced at the boundary. Hence, $\varepsilon|E|^2$ has a maximum just below the bottom of the NS. Such enhancement is effective for strengthening the light-matter interaction such as Purcell effect and strong coupling inside the semiconductor. In the completely perforated NS in (c), $\varepsilon|E|^2$ is concentrated in the NS and enhanced by a factor of 6.4. The maximum enhancement is expected for ultimately narrow NS by a factor of ε, i.e. $(n_{slab}/n_{air})^2 \sim 3.4^2 = 11.6$. Such localization is suitable for light-matter interaction outside of semiconductor [51]-[54], for sensing [55], [56] and for trapping [57].

Fig. 21 summarizes V_m and Q_{dif} as a function of d_{NS}/t. Gray and white regions correspond to the condition that the mode peak is located in the semiconductor and in the NS, respectively. The minimum V_m is $0.08(\lambda/n_{slab})^3 = 0.002(\lambda/n_{air})^3$ at d_{NS}/t = 0.4 – 0.6. V_m in the perforated type is three times larger than this minimum and 1.5 times larger than that without NS. This

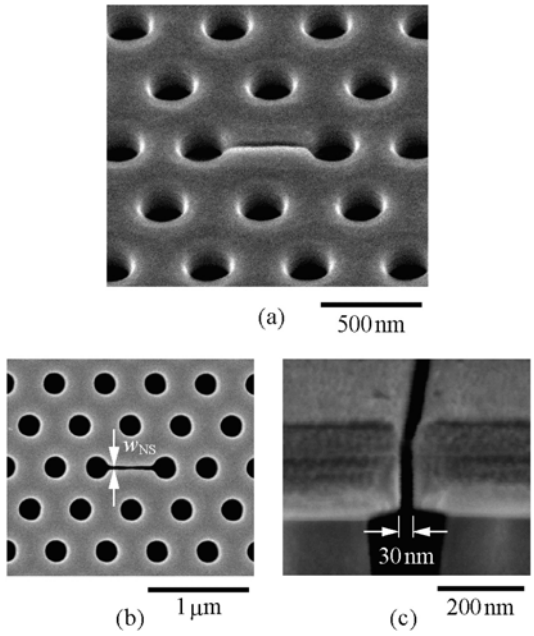

Fig. 23 (a) Bird's-eye view, (b) top view and (c) side view of the fabricated NS H0 nanolaser.

means that although the strong light localization is observed in the NS, other field is extending over a relatively wider area of semiconductor than the case without NS. Meanwhile, Q_{dif} constantly decreases as d_{NS}/t increases. The partial NS in Fig. 20(b) maintains a high Q_{dif} of ~10^4. This value is further degraded in the perforated NS, but pulsed lasing is still possible. Fig. 22 displays the electromagnetic field and energy distributions and its spatial FT in water for perforated NS devices, comparing the results for with and without optimization of airhole shifts. The mode is equally localized in the NS, but Q in water is improved and V_m is reduced with s_x and s_y tuning. For example, Q = 1300 and $V_m = 0.021(\lambda/n_{water})^3$ for the starting structure, while Q = 10,000 and $V_m = 0.006(\lambda/n_{water})^3$ for the optimized structure, even when the absorption of water is taken into account. The calculation also suggests that $w_{NS}/a < 0.12$ (e.g. w_{NS} < 60 nm for a = 0.5 μm) is necessary for such moderately high Q.

(b) Fabrication and laser operation

Fig. 23 shows SEM pictures of perforated NS device fabricated into the SQW wafer. Note that such a narrow NS of w_{NS} = 30 nm can be formed with the same resist thickness and etching condition, as described in Section III. To our knowledge, this is the narrowest NS ever reported for any devices and materials. In the HI ICP etching, the airholes pass through the GaInAsP active layer as well as the top and bottom InP layers, typically with a total depth of 1 μm. This means that a high aspect ratio of 30 is achieved in this etching.

The optical characterization is performed in a similarity to that described in Section IV. With sensor applications in mind, the device is operated in water. As mentioned above, the modal field in semiconductor extends further than the case without the NS. Therefore, the pump efficiency is too low and the laser operation is not observed with the same pump spot as for Fig. 11. We exchange the pump source to a high power type at λ =

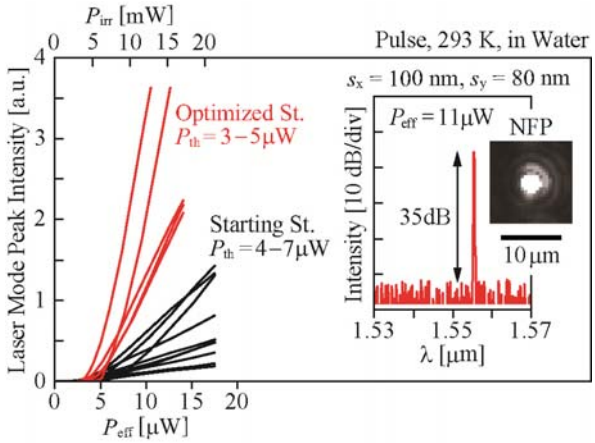

Fig. 24 Measured P_{out}–P_{eff} and P_{irr} plots for many NS nanolasers with and without structural optimization and laser spectrum above threshold in water for optimized structure. The near field pattern (NFP) of light output is also shown.

0.98 μm with multimode fiber output. The spot diameter on the device is 25 μm. It is difficult to obtain cw operation, because heating outside of the cavity is severe for such a large pump spot. Therefore, the measurement is done under pulsed condition (500 ns pulse width, 10 kHz repetition frequency). Fig. 24 shows the laser characteristics for many NS devices with w_{NS} = 30 – 60 nm. Here, P_{eff} only gives a rough measure because it is estimated for a modal area three times larger than that used for Fig. 11, considering the expansion of V_m. The results are compared between with and without s_y (= 60 – 120 nm). Clear lasing operation in water is observed for both of them, with 35 dB peak intensity. Devices with s_y exhibit lower threshold powers and higher slope efficiencies than those without s_y. Fig. 25 shows the unique spectral behaviors of this nanolaser. (a) compares the temperature dependence of lasing wavelength shift $\Delta\lambda_\ell$ between with and without the NS. The shift increases linearly with temperature T without NS. On the other hand, the dependence $\Delta\lambda_\ell / \Delta T$ is reduced to 0.17 times at T = 20 – 30ºC and almost eliminated at 40ºC with the NS. This can be explained as the influence of light localization in the NS filled with water. It is known that water has a negative TO coefficient of approximately -10^{-4} RIU/K at 20ºC [58]. Therefore, the positive TO effect of the semiconductor can be canceled. Water also has quadratic dependence that enhances the canceling effect at a higher temperature. Solid lines in Fig. 25(a) are obtained by taking account of these effects with the modal profile in Fig. 22. They explain the experimental behaviors very well, and the saturation in $\Delta\lambda_\ell$ indicates the athermal point. Based on this athermalization, the spectrum under the pulsed condition drastically narrows, as shown in (b). The gray line shows that without NS. As discussed in Section IV, the broad spectrum of $\Delta\lambda_s$ > 0.5 nm is determined by the temporal heating and heat diffusion in water. In contrast, the NS device exhibits a sharp spectrum of $\Delta\lambda_s$ = 18 pm due to the athermalization. This value is smaller than that without the NS under cw condition, and is close to the resolution limit of the OSA. (c) summarizes the power dependence of $\Delta\lambda_s$ at four different temperatures and different pulse widths Δt. The detail of each dependence exhibits irregular increase and decrease of $\Delta\lambda_s$ with the time-averaged pump power P_{ave}. It might be due to

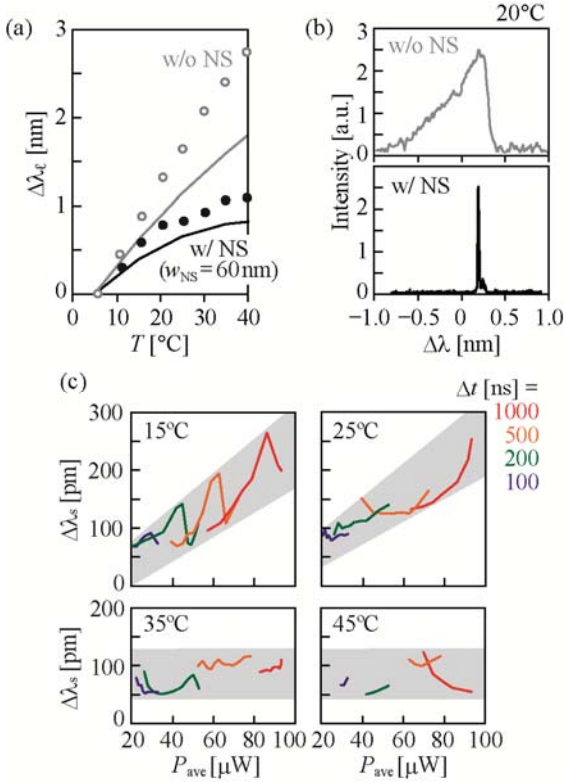

Fig. 25 Temperature dependence of spectral characteristics. (a) Wavelength shift $\Delta\lambda_\ell$ versus device temperature T in water. Solid lines and circular plots show theoretical and experimental values, respectively. Black and gray lines/circles denote with and without NS, respectively. (b) Comparison of lasing spectra in water between without and with NS. w_{NS} of the NS device is the same as in (a). (c) $\Delta\lambda_s$ as a function of P_{ave} at different temperatures and different pump pulse widths.

variation of the balance between the heating strength and TO coefficient and/or the deformation of the pump pulse. However, $\Delta\lambda_s$ roughly increases linearly with P_{ave} at lower temperatures, while the dependence almost disappears at higher temperatures. These results are consistent with each other, and indicate that the mode is localized in the NS as expected theoretically.

(c) Sensing characteristics

There are three important advantages in the NS nanolaser for sensing. First, the modal field localized in the NS enhances the sensitivity against the medium infiltrated and/or attached in the NS. Secondly the field in the NS is particularly intensified near the surface of the semiconductor. It is not clearly displayed in Figs. 20 and 22 because of the limited spatial resolution of calculations. However, it is expected from the discussion on the fundamental mechanism of light localization in the NS [47], [50]. Such field is particularly sensitive to a medium adsorbed at the surface, such as bio-molecules. Thirdly the linewidth $\Delta\lambda_s$ is greatly narrowed in water and other liquids having a negative TO coefficient, as shown above. They improve the sensing resolution according to Eq. (2). Fig. 26 demonstrates the enhanced sensitivity measured using the index liquids. (a) compares the spectral shift in different liquids with and without the NS; the shift is obviously wider with the NS. (b) summarizes the dependence of the sensitivity on w_{NS}. A higher sensitivity of 410 nm/RIU is obtained at w_{NS} = 75 nm,

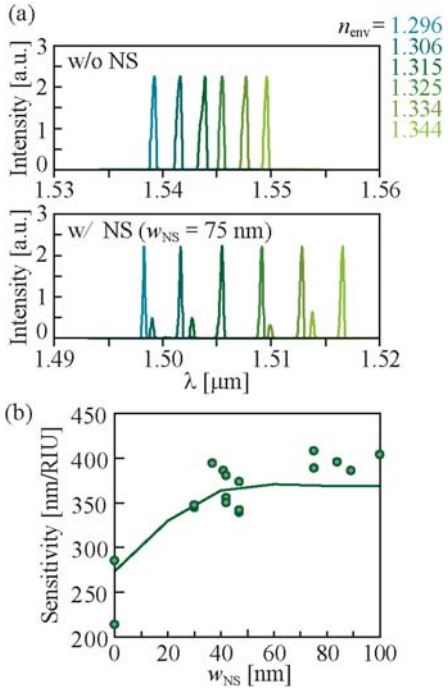

Fig. 26 Index sensitivity enhanced by NS in nanolasers. (a) Comparison of spectral shift in different index liquids with and without NS. (b) Dependence of sensitivity $\Delta\lambda_t/\Delta n_{env}$ on w_{NS}. Solid lines and circular plots show theoretical and experimental values, respectively.

which is a highest record for nanocavity-based sensors. The solid line shows the theoretical value obtained by the FDTD. The good agreement between experimental and theoretical results also supports the hypothesis that the modal field is enhanced in the NS. From the enhanced sensitivity and reduced linewidth, the index resolution is improved to 4.4×10^{-5} RIU, twice better than that for the cw device in Section IV.

VII. Conclusion

GaInAsP QW PC H0 nanolasers with and without NS of 30 – 100 nm width are fabricated simply by HI ICP etching, and operated by room temperature photopumping. With the optimized structural parameters, they exhibit an effective threshold of ~1 μW, clear mode intensity of 35 – 50 dB, good reproducibility and high yield. The theoretical and experimental results are very consistent with each other. From the consistency for NS devices, we confirm the strong mode localization in the NS. A large thermal resistance of 10^6 K/W order is a severe problem in nanolasers exposed to air. It brings a markedly wide thermal chirping of up to $\Delta\lambda_s$ = 10 nm under pulsed condition and 60 pm even under cw condition. The thermal chirping is suppressed in liquids to 0.5 – 1.0 nm and 26 pm, respectively. The localized field of the NS device in water allows the further narrowing of $\Delta\lambda_s$ to 18 pm under pulsed condition due to the cancelling of TO effect in semiconductor and water.

From these experimental results, we conclude that the nanolasers are suitable for sensing applications. Considering their essential narrow spectrum, high sensitivity particularly with NS, simple optical I/O and spectral analysis, and potential for low cost production even by using *e*-beam lithography, they are promising candidates as high-performance disposal sensor chips. In preliminary experiments, we evaluated an index resolution of 10^{-5} order in a single device using OSA and 10^{-3} order in arrayed device without using OSA. In particular, NS devices show higher sensitivities, narrow linewidths under pulsed condition, and athermal properties. They are not only effective for sensing liquids but also bio-molecules, which has been presented elsewhere [59].

Acknowledgment

This work was partly supported by the Grant-in-Aid #21246014 and a Research Fellowship from the Japan Society for the Promotion of Science (JSPS).

References

[1] O. Painter, J. Vučković and A. Scherer, "Defect modes of a two-dimensional photonic crystal in an optically thin dielectric slab," *J. Opt. Soc. Am.* B, vol. 16, pp. 275–285, Feb 1999.

[2] M. Lončar, T. Yoshie, A. Scherer, P. Gogna and Y. Qiu, "Low-threshold photonic crystal laser," *Appl. Phys. Lett.*, vol. 8, pp. 2680–2682, Oct 2002.

[3] H. Y. Ryu, S. H. Kwon, Y. J. Lee, Y. H. Lee and Jeong-Soo Kim, "Very-low-threshold photonic band-edge lasers from free-standing triangular photonic crystal slabs," *Appl. Phys. Lett.*, vol. 80, pp. 3476–3478, May 2002.

[4] T. Baba, D. Sano, K. Nozaki, K. Inoshita, Y. Kuroki and F. Koyama, "Observation of fast spontaneous emission decay in GaInAsP photonic crystal point defect nanocavity at room temperature," *Appl. Phys. Lett.*, vol. 85, pp. 3989–3991, Nov 2004.

[5] M. Nomura, S. Iwamoto, K. Watanabe, N. Kumagai, Y. Nakata, S. Ishida and Y. Arakawa, "Room temperature continuous-wave lasing in photonic crystal nanocavity," *Opt. Express*, vol. 14, pp. 6308–6315, Jun 2006.

[6] K. Nozaki, S. Kita and T. Baba, "Room temperature continuous wave operation and controlled spontaneous emission in ultimately small photonic crystal nanolaser," *Opt. Express*, vol. 15, pp. 7506–7514, Jun 2007.

[7] S. L. McCall, A. F. J. Levi, R. E. Slusher, S. J. Pearton and R. A. Logan, "Whispering gallery mode microdisk lasers," *Appl. Phys. Lett.*, vol. 60, pp. 289–291, Jun 1992.

[8] T. Baba, M. Fujita, A. Sakai, M. Kihara and R. Watanabe, "Lasing characteristics of GaInAsP/InP strained quantum-well microdisk injection lasers with diameter of 2 – 10 μm," *IEEE Photon. Technol. Lett.*, vol. 9, pp. 878–880, Jul 1997.

[9] K. Ohtaka, "Energy band of photons and low-energy photon diffraction," *Phys. Rev. B*, vol. 19, pp. 5057–5067, May 1979.

[10] E. Yablonovitch and T. J. Gmitter, "Inhibited spontaneous emission in solid state physics and electronics," *Phys. Rev. Lett.*, vol. 58, pp. 2059–2062, May 1987.

[11] T. Baba, N. Fukaya and J. Yonekura, "Observation of light propagation in photonic crystal optical waveguides with bends," *Electron. Lett.*, vol. 35, pp. 654–655, Apr 1999.

[12] K. Iga, F. Koyama and S. Kinoshita, "Surface emitting semiconductor lasers," *IEEE J. Quantum Electron*., vol. 24, pp. 1845–1855, Sep 1988.

[13] C. Böckler, S. Reitzenstein, C. Kistner, R. Debusmann, A. Löffler, T. Kida, S. Höfling, A. Forchel, L. Grenouillet, J. Claudon and J. M. Gérard, "Electrically driven high-Q quantum dot-micropillar cavities," *Appl. Phys. Lett.*, vol. 92, pp. 091107-1–091107-3, Mar 2008.

[14] S. L. McCall, A. F. J. Levi, R. E. Slusher, S. J. Pearton and R. A. Logan, "Whispering-gallery mode microdisk lasers," *Appl. Phys. Lett.*, vol. 60, pp. 289–291, Jan 1992.

[15] A. F. J. Levi, R. E. Slusher, S. L. McCall, T. Tanbunek, D. L. Coblentz and S. J. Pearton, "Room-temperature operation of microdisk lasers with submilliamp threshold current," *Electron. Lett.*, vol. 28, pp. 1010–1012, May 1992.

[16] T. Baba, "Photonic crystals and microdisk cavities based on GaInAsP-InP system," *IEEE J. Sel. Top. Quantum Electronics*, vol. 3, pp. 808–830, Jun 1997.

[17] M. Kuwatagonokami, R. H. Jordan, A. Dodabalapur, H. E. Katz, M. L. Schilling and R. E. Slusher, "Polymer microdisk and microring lasers," *Opt. Lett.,* vol. 20, pp. 2093–2095, Oct 1995.

[18] K. Nozaki, A. Nakagawa, D. Sano and T. Baba, "Ultralow threshold and singlemode lasing in microgear lasers and its fusion with quasiperiodic photonic crystals," *IEEE J. Sel. Top. Quantum Electron.*, vol. 9, pp. 1355−1360, Oct 2003.

[19] K. D. Vos, I. Bartolozzi, E. Schacht, P. Bienstman and R. Baets, "Silicon-on-Insulator microring resonator for sensitive and label-free biosensing," *Opt. Express*, vol. 15, no. 12, pp. 7610−7615, Jun 2007.

[20] D. K. Armani, T. Kippenberg, S. M. Spillane and K. J. Vahala, "Ultra-high-Q toroid microcavity on a chip," *Nature*, vol. 421, pp. 925−929, Feb 2003.

[21] A. M. Armani, R. P. Kulkarni, S. E. Fraser, R. C. Flagan and K. J. Vahala, "Label-free, single-molecule detection with optical microcavities," *Science*, vol. 317, pp. 783−787, Aug 2007.

[22] M. L. Gorodetsky, A. A. Savchenkov and V. S. Ilchenko, "Ultimate Q of optical microsphere resonators," *Opt. Lett.,* vol. 21, pp. 453–455, Apr 1996.

[23] N. M. Hanumegowda, C. J. Stica, B. C. Patel, I. White and X. Fan, "Refractometric sensors based on microsphere resonators," *Appl. Phys. Lett.*, vol. 87, pp. 201107-1–201107-3, Nov 2005.

[24] K. Srinivasan and O. Painter, "Momentum space design of high-*Q* photonic crystal optical cavities," *Opt. Exp*ress, vol. 10, pp. 670–684, Jul 2002.

[25] Z. Zhang and M. Qiu, "Small-volume waveguide-section high *Q* microcavities in 2D photonic crystal slabs," *Opt. Express,* vol. 12, pp. 3988−3995, Aug 2004.

[26] K. Nozaki, T. Ide, J. Hashimoto, W. H. Zheng and T. Baba, "Photonic crystal point shift nanolaser with ultimate small modal volume," *Electron. Lett.* vol. 41, pp. 843–845, Jul 2005.

[27] K. Nozaki, T. Tanabe, A. Shinya, S. Matsuo, T. Sato, H. Taniyama and M. Notomi, "Sub-femtojoule all-optical switching using a photonic-crystal nanocavity," *Nature Photonics*, vol. 4, pp. 477–483, Jul 2010.

[28] S. Kita, K. Nozaki and T. Baba, "Refractive index sensing utilizing a cw photonic crystal nanolaser and its array configuration", *Opt. Express*, vol. 16, pp. 8174–8180, May 2008.

[29] K. Nozaki, S. Kita, Y. Arita and T. Baba, "Resonantly photopumped lasing and its switching behavior in a photonic crystal nanolaser," *Appl. Phys. Lett.*, vol. 92, pp. 021501-1–021501-3, Jan 2008.

[30] K. Nozaki, H. Watanabe and T. Baba, "Photonic crystal nanolaser monolithically integrated with passive waveguide for effective light extraction," *Appl. Phys. Lett.*, vol. 92, pp. 021108-1–021108-3, Jan 2008.

[31] T. Baba, K. Inoshita, H. Tanaka, J. Yonekura, M. Ariga, A. Matsutani, T. Miyamoto, F. Koyama, and K. Iga, "Strong enhancement of light extraction efficiency in GaInAsP 2-D-arranged microcolumns," *J. Lightwave Technol.*, vol. 17, pp. 2113–2120, Nov 1999.

[32] A. Forchel, P. Ils, K. H. Wang, O. Schilling, R. Steffen, and J. Oshinowo, "Quantum wires and dots for optical studies," *Microelectronic Engineering*, vol. 32, pp. 317–330, Sep 1996.

[33] H. Watanabe and T. Baba, "High-efficiency photonic crystal microlaser integrated with a passive waveguide", *Opt. Express*, vol. 16, pp. 2694–2698, Feb 2008.

[34] S. Matsuo, A. Shinya, T. Kakitsuka, K. Nozaki, T. Segawa, T. Sato, Y. Kawaguchi and M. Notomi, "High-speed ultracompact buried heterostructure photonic-crystal laser with 13 fJ of energy consumed per bit transmitted," *Nature Photonics*, vol. 4, pp. 648–654, Sep 2010.

[35] K. Inoshita and T. Baba, "Fabrication of GaInAsP/InP photonic crystal lasers by ICP etching and control of resonant mode in point and line composite defects," *IEEE J. Sel. Top. Quantum Electron.* vol. 9, pp. 1347–1354, Sep 2003.

[36] K. Nozaki and T. Baba, "Carrier and photon analyses of photonic microlasers by two-dimensional rate equations," *IEEE J. Sel. Area. Commun.*, vol. 23, no. 7, pp. 1411−1417, Jul 2005.

[37] Y. Takahashi, H. Hagino, Y. Tanaka, B. S. Song, T. Asano and S. Noda, "High-Q nanocavity with a 2-ns photon lifetime," *Opt. Express*, vol. 15, pp. 17206−17213, Dec 2007.

[38] H. Hagino, Y. Takahashi, Y. Tanaka, T. Asano, and S. Noda, "Effects of fluctuation in air hole radii and positions on optical characteristics in photonic crystal heterostructure nanocavities," *Phys. Rev. B,* vol. 79, pp. 085112-1–085112-8 Feb 2009.

[39] T. Yoshie, M. Lončar, A. Scherer and Y. Qiu, "High frequency oscillation in photonic crystal nanolaser," *Appl. Phys. Lett.*, vol. 84, pp. 3543−3545, May 2004.

[40] H. Watanabe, K. Nozaki and T. Baba, "Very wide wavelength chirping in photonic crystal nanolaser," *Int. Sympo. Compound Semiconductors* (Kyoto), no. TuC P-10, Oct 2007.

[41] R. Ushigome, M. Fujita, A. Sakai, T. Baba and Y. Kokubun, "GaInAsP microdisk injection laser with benzocyclobutene polymer cladding and its athermal effect," *Jpn. J. Appl. Phys.*, vol. 41, pp. 6364–6369, Nov 2002.

[42] M. Lončar, A. Scherer and Y. Qiu, "Photonic crystal laser sources for chemical detection," *Appl. Phys. Lett.*, vol. 82, pp. 4648−4650, Jun 2003.

[43] M. R. Lee and P. M. Fauchet, "Two-dimensional silicon photonic crystal based biosensing platform for protein detection," *Opt. Express*, vol. 15, pp. 4530−4535, Apr 2007.

[44] M. Adams, G. A. DeRose, M. Lončar and A. Scherer, "Lithographically fabricated optical cavities for refractive index sensing," *J. Vac. Sci. Technol. B*, vol. 23, pp. 3168−3173, Dec 2005.

[45] S. H. Kim, J. H. Choi, S. K. Lee, S. H. Kim, S. M. Yang, Y. H. Lee, C. Seassal, P. Regrency and P. Viktorovitch, "Optofluidic integration of a photonic crystal nanolaser," *Opt. Express*, vol. 16, pp. 6515−6527, Apr 2008.

[46] G. M. Hale and M. R. Querry, "Optical constants of water in the 200-nm to 200-μm wavelength region," *Appl. Opt.,* vol. 12, pp. 555−563, 1973.

[47] V. R. Almeida, Q. F. Xu, C. A. Barrios and M. Lipson, "Guiding and confining light in void nanostructure," *Opt. Lett.*, vol. 29, pp. 1209−1211, Jun 2004.

[48] Q. F. Xu, V. R. Almeida, R. R. Panepucci and M. Lipson, "Experimental demonstration of guiding and confining light in nanometer-size low-refractive-index material," *Opt. Lett.*, vol. 29, pp. 1626−1628, Jul 2004.

[49] C. A. Barrios and M. Lipson, "Electrically driven silicon resonant light emitting device based on slot-waveguide," *Opt. Express*, vol. 13, pp. 10092−10101, Dec 2005.

[50] J. T. Robinson, C. Manolatou, L. Chen and M. Lipson, "Ultrasmall mode volumes in dielectric optical microcavities," *Phys. Rev. Lett.*, vol. 95, pp. 145901-1−145901-4, Sep 2005.

[51] J. M. Gerard, B. Sermage, B. Gayral, B. Legrand, E. Costard and V. Thierry-Mieg, "Enhanced spontaneous emission by quantum boxes in a monolithic optical microcavity," *Phys. Rev. Lett.*, vol. 81, pp. 1110−1113, Aug 1998.

[52] J. M. Gerard and B. Gayral, "Strong purcell effect for InAs quantum boxes in three-dimensional solid-state microcavities," *J. Lightwave Technol.*, vol. 17, pp. 2089–2095, Nov 1999.

[53] T. Yoshie, A. Scherer, J. Hendrickson, G. Khitrova, H. M. Gibbs, G. Rupper, C. Ell, O. B. Shchekin and D. G. Deppe, "Vacuum Rabi splitting with a single quantum dot in a photonic crystal nanocavity," *Nature*, vol. 432, pp. 200−203, Nov 2004.

[54] N. A. Mortensen, S. S. Xiao and J. Pedersen, "Liquid-infiltrated photonic crystals: enhanced light-matter interactions for lab-on-a-chip applications," *Microfluidics and Nanofluidics*, vol. 4, pp. 117−127, Jan 2008.

[55] C. A. Barrios, M. J. Banuls, V. Gonzalez-Pedro, K. B. Gylfason, B. Sanchez, A. Griol, A. Maquieira, H. Sohlstrom, M. Holgado and R. Casquel, "Label-free optical biosensing with slot-waveguides," *Opt. Lett.*, vol. 33, pp. 708−710, Apr 2008.

[56] A. Di Falco, L. O'Faolain and T. F. Krauss, "Chemical sensing in slotted photonic crystal heterostructure cavities," *Appl. Phys. Lett.*, vol. 94, Feb 2009.

[57] A. H. J. Yang, S. D. Moore, B. S. Schmidt, M. Klug, M. Lipson and D. Erickson, "Optical manipulation of nanoparticles and biomolecules in sub-wavelength slot waveguides," *Nature*, vol. 457, pp. 71−75, Jan 2009.

[58] D. R. Lide, CRC Handbook of Chemistry and Physics, *CRC PRESS*, 82nd ed., Boca Raton, 2001, p. 10-218.

[59] S. Kita, S. Hachuda T. Endo, Y. Nishijima, H. Misawa and T. Baba, "High-sensitivity biosensing using nanolaser," *IEEE Sensors Conf.*, (Hawaii), no. C1L-E6, Nov 2010.

Shota Kita received the B. E. and M. E. degrees from the Department of Electrical and Computer Engineering, Yokohama National University, Yokohama, Japan, in 2007 and 2009, respectively. He is currently working towards the Ph. D. degree in photonic crystal nanolasers and their applications for sensing liquids and bio-molecules at the same university. Mr. Kita is a member of the Japan Society of Applied Physics.

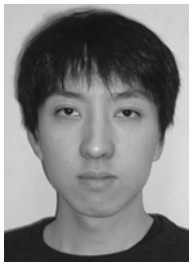

Kengo Nozaki received the B. E., M. E., and Ph. D. degrees all from the Department of Electrical and Computer Engineering, Yokohama National University, Japan, in 2003, 2005 and 2008, respectively. During his Ph. D. work, he had been engaged in photonic crystal and quasi-crystal nanolasers and their spontaneous emission control. In 2007, he has achieved the first room temperature cw operation in the nanolasers. He joined NTT Basic Research Laboratories in 2008 as a researcher. He recently reported an ultrasmall photonic crystal optical switch operating at 40 Gbps speed with a sub-fJ switching energy, and its flip-flop operation enabling entire memory of optical signal. Dr. Nozaki is a member of the Japan Society of Applied Physics. He received the Niwa Memorial Prize in 2008.

Shoji Hachuda received the B. E. degree from the Department of Electrical and Computer Engineering, Yokohama National University, Yokohama, Japan, in 2010. He is currently working towards the M. D. degree in bio-electronics and surface chemistry at the same university. Mr. Hachuda is a member of the Japan Society of Applied Physics.

Hideki Watanabe received the B. E. and M. E. degrees from the Department of Electrical and Computer Engineering, Yokohama National University, Yokohama, Japan, in 2006 and 2008, respectively. During his study, he successfully integrated photonic crystal microlaser and waveguide and achieved a high external efficiency. He also investigated the thermal chirping in photonic crystal nanolaser and amplification in photonic crystal waveguides. Currently he is with Sony Corp. and studying mode-locked semiconductor lasers in GaN system.

Yuji Saito received the B. E. and M. E. degrees from the Department of Electrical and Computer Engineering, Yokohama National University, Yokohama, Japan, in 2008 and 2010, respectively. He has studied the thermal chirping in photonic crystal nanolasers. Currently he is working towards the Ph. D. degree in generation of stopped light by the dynamic tuning of photonic crystal waveguides. Mr. Saito is a member of the Japan Society of Applied Physics.

Shota Otsuka received the B. E. degree from the Department of Electrical and Computer Engineering, Yokohama National University, Yokohama, Japan, in 2011. He is currently working towards the M. D. degree in bio-sensing using photonic crystal nanolasers at the same university. Mr. Otsuka is a member of the Japan Society of Applied Physics.

Takeharu Nakada received the B. E. and M. E. degrees from the Department of Electrical and Computer Engineering, Yokohama National University, Yokohama, Japan, in 2007 and 2009, respectively. During his study, he investigated the amplification in photonic crystal waveguides. Currently he is with Cannon Corp.

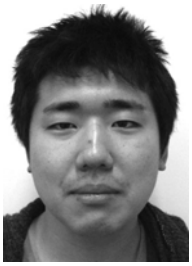

Yoshiki Arita received the B. E. and M. E. degrees from the Department of Electrical and Computer Engineering, Yokohama National University, Yokohama, Japan, in 2008 and 2010, respectively. During his study, he investigated functional devices based on photonic crystal nanolaser coupled with waveguides, pulse train generator and tunable delay line in silicon photonics, and optical bus with SFQ superconductor circuits. Currently he is with Shimazu Corp. Mr. Aria is a member of the Japan Society of Applied Physics.

Toshihiko Baba (M'03) received the Ph. D. degree from the Division of Electrical and Computer Engineering, Yokohama National University (YNU), Japan, in 1990. During his Ph. D. work, he had been engaged in on-Si waveguides, ARROW waveguides, and 3D photonic integration. From 1991 – 1993, he joined Tokyo Institute of Technology as a research associate. He discussed the spontaneous emission control in VCSELs and achieved the room temperature cw operation in a long wavelength device. He became an associate professor and full professor of YNU in 1994 and 2005, respectively. In these 15 years, he has studied photonic nanostructures such as photonic crystals (PCs), high-index-contrast structures, and Si photonics. He first demonstrated PC waveguides, surface-PC LEDs, and Si photonic wire components. He also achieved the room temperature cw operation in PC nanolasers and microdisk lasers with the strong Purcell effect, record high single-mode power holey VCSEL, negative refractive components for lightwaves, and ultra-compact Si AWG demultiplexer. His recent study is focusing on slow light in PC waveguides towards optical buffering and nonlinear enhancement. Dr. Baba is a member of the Institute of Electronics, Information and Communication Engineers, the Japan Society of Applied Physics, Optical Society of America, and American Physics Society. He received nine academic awards including JSPS Award in 2005 and LEOS Distinguished Lecturer Award in 2006-2007.